Two-element interferometer fringe measurements at 10.7 GHz

Aaron Tran[1,2,3]

Leonardo S. Cassara[1,2], Ryan (Xin Xing) Gao[1,2], Patrick Kantorski[1,2], Salman Kahn[1,4]
Aaron Parsons[2,5,6], Garrett K. Keating[2,5,6], Baylee Bordwell[2,6]

[1]PLSAR Collaboration
[2]Dept. Astronomy, UC Berkeley, D-23 Hearst Field Annex, Berkeley, CA 94720, USA
[3]Dept. Earth and Planetary Science, UC Berkeley, 335 McCone Hall, Berkeley, CA 94720, USA
[4]Dept. Physics, UC Berkeley, 251 LeConte Hall, Berkeley, CA 94720, USA
[5]Radio Astronomy Laboratory, UC Berkeley, Berkeley, CA 94720, USA
[6]Undergraduate Radio Laboratory teaching staff

Abstract

We measure sun and moon angular diameters of $\sim$ 0.5–0.7° by matching zero crossings in expected modulation functions with fringe envelope curve minima.

Keywords: astrometry — instrumentation: interferometers — galaxies: individual (NGC 4486) — ISM: individual (NGC 1976, NGC 6618)

1 Introduction

Motivation – measure source declinations and sun moon angular diameters Pedagogical – understand interferometry Least squares fitting to back out meaningful astronomical numbers

Roadmap: rotation matrices for calculation and ephemerides Interferometer design Interferometer signal (averaging, frequency components) Least squares fitting dec/baseline Leasts squares fitting diameter Conclusion

2 Review of astronomical time and coordinates

We review astronomical timekeeping and coordinate systems used in this study: sidereal time, Julian dates, right ascension and declination, and altitude-azimuth coordinates. A far more thorough and pedagogical presentation is given by *Green* [1985]. For sanity's sake, I assume the reader is acquainted with geographical and celestial coordinates.

Julian date quantifies solar time; a Julian day is 86400 seconds and a Julian year is 365.25 days. The timescales used to measure Julian dates may vary (e.g. ephemeris time, terrestrial dynamical time) and are difficult to decipher. *Sidereal time* quantifies Earth's rotation relative to the fixed stars. As viewed from Earth, the fixed stars take one *sidereal day* (23h, 56m, 4s of solar time) to sweep out 360° longitude on the celestial sphere. A sidereal day is slightly shorter than a solar day due to the Earth's orbital motion around the Sun, and, to a much lesser extent, precession and nutation of the Earth's rotation axis. *Local sidereal time* (LST) is sidereal time adapted for a specific location (longitude) on Earth, and is defined by the vernal equinox's hour angle (HA).

Astronomical positions are specified by location-agnostic spherical coordinates, typically *right ascension* (RA, α) and *declination* (dec, δ). To perform observations, we convert (α, δ) into more useful coordinates for given geographic latitude and longitude – namely, *altitude* and *azimuth* (alt, az). Our presentation of the requisite coordinate transformation follows that of Carl Heiles.

Let (x, y, z) specify a right-handed coordinate system where the polar angle is measured relative to the z-axis and the azimuth is measured in the x-y plane starting from the positive x-axis. In (α, δ) coordinates, the Earth's rotation axis and equatorial plane correspond to the z-axis and x-y plane respectively (i.e., right ascension and declination specify a geocentric equatorial coordinate system). Right ascension is measured counter-clockwise about the z-axis starting from the vernal equinox's position on the celestial sphere (positive

1

x-axis). Declination is measured upwards (towards positive z) from the equatorial (x-y) plane. We see that declination corresponds to the usual polar angle, and right ascension to azimuthal angle.

We compute coordinate transformations using rotation matrices in Cartesian coordinates. Our coordinate transformations act upon Cartesian coordinate bases from which we measure polar and azimuthal angles for (RA, dec), (HA, dec), and (alt, az) coordinates (e.g., our previously defined x, y, z); these transformations are deemed "passive" as they only alter the coordinate representations of physical vectors. A unit vector in (α, δ) coordinates may be written in Cartesian coordinates as:

$$(x, y, z) = (\cos \alpha \cos \delta, \sin \alpha \cos \delta, \sin \delta)$$

We select a longitude by converting right ascension (α) to hour angle (HA):

$$\text{HA} = \text{LST} - \alpha$$

This transformation is a rotation about the z-axis and a reflection across the x-z plane; (HA, δ) coordinates have reversed handedness compared to (α, δ) and the rotated x-axis is perpendicular to the meridian at which we evaluate LST, HA. The new coordinate basis has Cartesian representation:

$$(x', y', z') = (\cos(\text{HA}) \cos \delta, \sin(\text{HA}) \cos \delta, \sin \delta)$$

Two more rotations convert (HA, δ) to (alt, az). We rotate the x'-z' plane by $(\phi - \pi/2)$, where ϕ is geographic latitude, then rotate the transformed x'-y' plane by π radians. The rotation matrix is constructed as:

$$\begin{pmatrix} \cos(\pi) & \sin(\pi) & 0 \\ \sin(\pi) & \cos(\pi) & 0 \\ 0 & 0 & 1 \end{pmatrix} \begin{pmatrix} \cos(\phi - \pi/2) & 0 & \sin(\phi - \pi/2) \\ 0 & 1 & 0 \\ \sin(\phi - \pi/2) & 0 & \cos(\phi - \pi/2) \end{pmatrix} = \begin{pmatrix} -\sin \phi & 0 & \cos \phi \\ 0 & -1 & 0 \\ \cos \phi & 0 & \sin \phi \end{pmatrix}$$

The final coordinate basis has the same handedness as (HA, δ) coordinates and is written:

$$(x'', y'', z'') = (\cos(\text{az}) \cos(\text{alt}), \sin(\text{az}) \cos(\text{alt}), \sin(\text{alt}))$$

Altitude is measured upwards from the x''-y'' plane (i.e., the Earth's local tangent plane) and azimuth is measured clockwise from geographic north.

For arbitrary (α, δ), the topocentric Cartesian coordinates are:

$$\hat{s} = \begin{pmatrix} -\cos(\text{HA}) \sin \phi \cos \delta + \cos \phi \sin \delta \\ -\sin(\text{HA}) \cos \delta \\ \cos(\text{HA}) \cos \phi \cos \delta + \sin \phi \sin \delta \end{pmatrix} \tag{1}$$

These coordinate transformations correctly predict astronomical positions for both stationary celestial objects and Solar System objects. Our rotation matrices agree with PyEphem calculations to ~ 10 arcseconds; note that PyEphem's atmospheric refraction correction must be disabled. In this study, we use PyEphem to compute all coordinate transformations for observations and data analysis.

3 Methods

3.1 Interferometer design

We measure 10.7 GHz (X-band) emission using a two-element multiplying interferometer. The interferometer consists of two antennae (diameter $d \sim 1$ m) with east-west baseline $B \approx 10$ m on the rooftop of Wurster Hall, Univ. California Berkeley ($37°52'12.7''$ N, $-122°15'15.8''$ E). The interferometer beam size is $\lambda/d \sim 1.6°$ and angular resolution is $\lambda/B \sim 0.16°$. The stated bandwidth is 10 MHz, though we do not know the antenna response or the frequency band uncertainty of our interferometer dishes. We conservatively estimate the absolute frequency error to be ~ 100 MHz at worst.

The interferometer may point from 15° to 87° in altitude, and its northern field of view is obstructed by a taller portion of Wurster Hall. We estimate that Wurster Hall obstructs the sky between −20° and 10° azimuth and up to 40° altitude. All observations are performed within 17–85° altitude and outside the range of the Wurster Hall obstruction.

A fixed celestial object will move at most 15° per hour, or 0.125° every 30 s. We point the interferometer at 30 second intervals to keep point sources of interest within ∼ 0.13° (10% of interferometer beamwidth) of the interferometer beam's center. Encoders in the interferometer dishes must be reset ("homed") every 100 pointings to maintain angular positioning accuracy. Homing takes ∼ 1 minute for every 50 min. of observation. Interferometer data collected while homing appear as voltage spikes which we remove during data reduction.

3.2 Interferometer signal processing

The interferometer signal is heterodyne downconverted at the dishes to approximately 1.7 GHz, then to 150 MHz further along the signal path. The twice-downconverted signals are mixed and sampled at ∼ 1 Hz. Amplifiers and filters between downconverting mixers improve signal quality and restrict signal bandwidth to 10 MHz. But, we necessarily lose information about electric field amplitude at the interferometer dishes.

4 Observations

4.1 Observing campaign

We observed the Sun, the Moon, and the unresolved point sources NGC 1976 (Orion Nebula, M42), NGC 4486 (Virgo A, M87), and NGC 6618 (Omega Nebula, M17) (Table 1). The Moon was observed twice: once while waxing crescent with ∼ 20% illumination (2014 April 4), and once during a total lunar eclipse (2014 April 15). All observations are single horizon-to-horizon runs except our observation of the Orion Nebula.

Table 1. Summary of interferometer observations. Sun and moon flux densities are calculated with $T_b = 14600$ K, 217 K assuming uniform blackbody emission. Sun brightness temperature is average of estimates for sunspot cycle minima and maxima [*Hafez et al.*, 2014; *Salomonovich and Losovskii*, 1963].

Object	S_ν (Jy)	Observation start (UT)	Observation end (UT)
Sun	$\sim 4 \cdot 10^6$	2014 Apr 01 15:25:44	2014 Apr 02 01:02:20
Moon	$\sim 6 \cdot 10^4$	2014 Apr 04 18:54:38	2014 Apr 05 06:09:51
(eclipsed) Moon	$\sim 6 \cdot 10^4$	2014 Apr 15 04:09:22	2014 Apr 15 12:06:06
NGC 1976	~ 340	2014 Mar 21 22:53:18	2014 Mar 22 09:01:47
NGC 4486	~ 34	2014 Apr 03 03:03:15	2014 Apr 03 12:57:36
NGC 6618	~ 500	2014 Apr 05 10:07:34	2014 Apr 05 17:04:13

4.2 Data reduction

Dish homing takes ∼ 1 minute and introduces spurious voltage spikes as data collection continues during homing and subsequent re-pointing. We extract homing start and stop times from automatically generated observing logs and remove all data associated with homing and re-pointing (Figure 1a). The interferometer output also carries a fluctuating DC offset ($\Delta V \sim \pm 1$ mV) comparable to measured voltages for all sources except the sun; we are unable to explain the cause of this variable offset. We extract the DC offset signal with a 240 second wide boxcar filter and subtract the offset from the interferometer output. Figure 1 plots raw and reduced data for the 2014 April 4 moon observation.

We compute power spectra as a function of frequency from cleaned data using the discrete Fourier transform. For moon and sun observations, we observe a gradually increasing signal from 0.015–0.027 Hz consistent
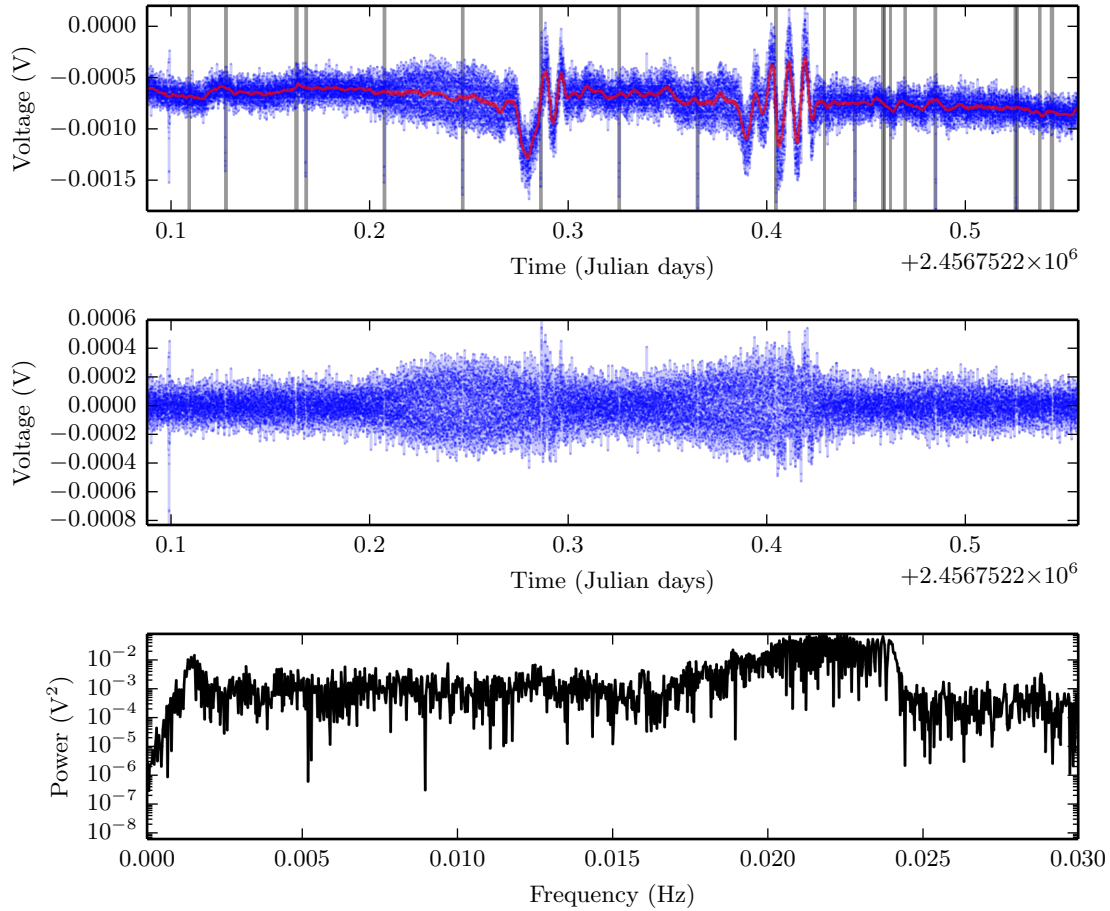
Figure 1. (top) Raw interferometer output from 2014 April 4 Moon observation; overlaid vertical lines identify homing spikes and gaps in data collection. (middle) Interferometer output with fluctuating DC offset and homing spikes removed. Data reduction allows fringe modulation to be recovered and extracted. (bottom) Partial power spectrum of reduced interferometer data.

with the range of expected fringe frequencies; in point source data, a weak and possibly spurious peak may be discerned near 0.027 Hz. We assume the sampling period is 1 second despite gaps in data sampling, introducing some error. Although we do not account for uneven sampling here, we refer the interested reader to work by *Dutt and Rokhlin* [1993] and *Ferraz-Mello* [1981].

5   Results

5.1   Interferometer point source response

The interferometer outputs the product of two voltage signals. For a point source, the interferometer response is proportional to:

$$F(t) = \cos(2\pi\nu t)\cos\left(2\pi\nu\left[t+\tau\right]\right)$$
$$\approx \cos\left(2\pi\nu\tau\right)$$

4

where the time delay $\tau = (B_y/c)\cos\delta\sin(h_s) + \tau_c$ sums geometric and cable delay and we have dropped a rapidly varying 22 GHz sum term. Splitting τ into cable and geometric delays gives:

$$F(t) = \cos(2\pi\nu\tau_c)\cos\left[2\pi\left(\frac{B_y}{\lambda}\cos\delta\right)\sin h_s\right] - \sin(2\pi\nu\tau_c)\sin\left[2\pi\left(\frac{B_y}{\lambda}\cos\delta\right)\sin h_s\right] \qquad (2)$$

As τ_c is a constant, the interferometer output is a sinusoid with variable frequency, determined by $\sin(h_s)$.

5.2 Declination measurement from fringe frequencies

We may infer either of interferometer baseline or source declination by non-linear least squares fitting our interferometer data to equation 2. Our non-linear fit involves three free parameters: $A \equiv \cos(2\pi\nu\tau_c)$, $B \equiv \sin(2\pi\nu\tau_c)$, and $k \equiv 2\pi\frac{B_y}{\lambda}\cos\delta$. We compute $x \equiv \sin h_s$ from the times and hence hour angles of all observations. The fit equation becomes:

$$F(t) = A\cos(kx) + B\sin(kx)$$

If a value of k is given, A and B are readily fit by linear least squares. We brute force the non-linear least squares fit in k as follows.
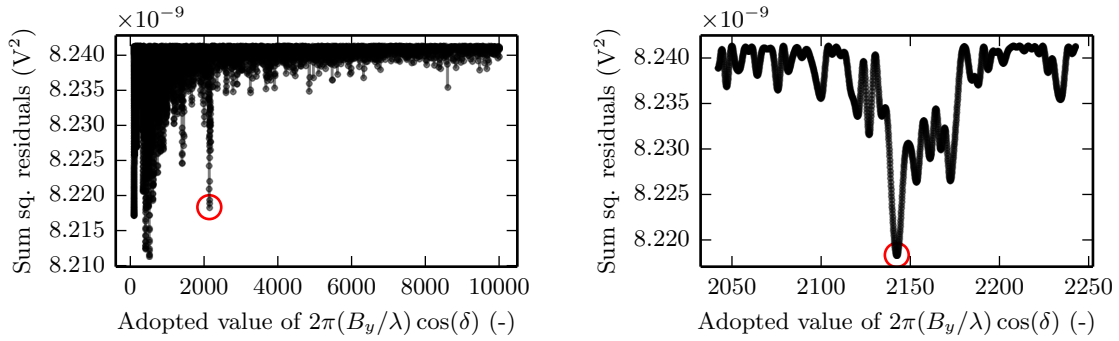

Figure 2. Scaled sum of squared residuals from linear fits for A, B as a function of $k = 2\pi\left(B_y/\lambda\right)\cos\delta$, fitting fringe data from NGC 6618 (M17); (left) a large range of possible k values with logarithmic sampling; (right) a smaller range of k values shows nearby minima. Red circles plot iteratively computed best-fit k. Note that ordinate (y) axes differ between the two plots.

We seek a value of k that minimizes the sum of squared residuals, computed from a linear fit to A, B. Start with an initial guess $k_i = 2000$ and search domain $k \in [1000, 3000]$ centered on k_i. Sample 1000 evenly spaced k values in this range and use each value to compute a linear least squares fit for A, B. Take the sampled k value with minimum sum of squared residuals as our next guess for k and halve the search domain. Iterate this procedure of guessing k and refining the search domain until two consecutive guesses for k differ by less than 0.0002 (i.e., fractional change $\sim 10^{-7}$ for $k \approx 2000$). Our procedure converges to a value of k within or near the initial search domain (Figure 2), although it is not guaranteed to converge to an absolute minimum within or near the search domain. Qualitatively, our procedure appears robust to variations in sampling and search domain.

Our fits are only marginally better than a straight line fit and cannot explain most sample variance (Figure 3). However, Figure 2 illustrates that a meaningful signal is present and can be robustly detected by our non-linear fitting procedure.

With a value for k in hand, we assume baseline $B = 10$ m and estimate the fit declination δ. We also perform the reverse procedure by calculating source declinations (epoch J2000, precessed to 2014 April 7 using PyEphem) and then estimate the fit baseline. We estimate the cable delay by computing $2\pi\nu\tau_c = \arctan(-B/A)$ (equation 2); however, the largest measurable cable delay is ± 47 ps as we can only measure signal phase offset. Table 2 summarizes our best fit parameters.
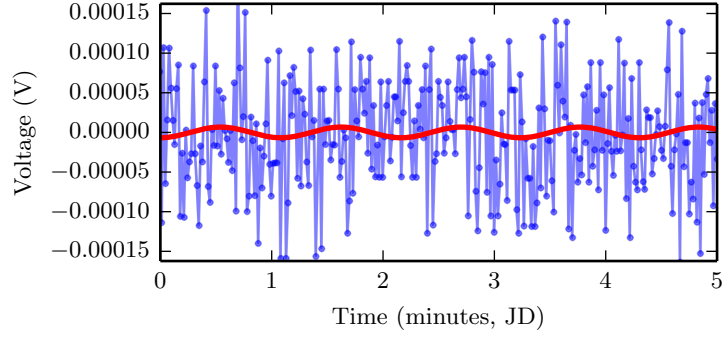
Figure 3. Red line plots equation 2 with best fit values for k, A, B from non-linear least squares fitting procedure; blue circles plot interferometer data from NGC6618 (M17), corresponding to fit k from Figure 2.

We estimate uncertainties in our fit values by taking $\nu = 10.7 \pm 0.1$ GHz and $B = 10 \pm 0.1$ m. We are unable to quantify uncertainty for our fitted value of k, although this is the most important possible source of systematic error. Interestingly, we expect a more precise measurement of δ with larger declination (farther from $\delta = 0$). Why? The function $\cos \delta$ is relatively insensitive to changes in δ near $\delta = 0$, hence uncertainty in $\cos \delta$ is propagated into a larger uncertainty in δ.

Table 2. Parameter estimates from brute force least squares

Object	Fit k (-)	Fit, actual δ (°)	Fit B (m)	Fit τ_c (ps)
NGC 1976 (Orion)	2227.45	$-6.7° \pm 7°, -5.34°$	9.98 ± 0.1	-27
NGC 4486 (Virgo A)	2077.17	$22.1° \pm 2°, 12.31°$	9.48 ± 0.1	42
NGC 6618 (M17)	2142.41	$-17.2° \pm 3°, -16.2°$	9.95 ± 0.1	34

The calculated declinations for NGC 1976 (Orion) and NGC 6618 (M17) are accurate to about $1°$ on the sky, whereas our estimate of declination for NGC 4486 is off by $10°$. Similarly, the calculated baselines for Orion and M17 agree with expectation to within 0.1 m. We attribute the poor parameter fits for Virgo A to comparatively weak signal strength; the flux density of Virgo A at 10.7 GHz is an order of magnitude weaker than flux densities for Orion and M17.

5.3   Angular diameters of the Sun, Moon

We now examine the interferometer response to extended sources in the sky, which is proportional to:

$$R(h_s) = \int I_\nu(\Delta h) \cos(2\pi\nu\tau_{\text{tot}})d(\Delta h)$$

Here h_s is the hour angle of the extended source's center, and $\Delta h = h - h_s$ is hour angle h measured relative to our source. This is simply the visibility equation with a cosine Fourier transform from our signal mixing, integrated over a 1-D sky. We may think of this equation as integrating the impulse response over source extent; for $I_\nu(h_s) = \delta(\Delta h)$, we recover the usual fringe response $F(h_s) = \cos(2\pi\nu\tau_{\text{tot}})$. Conveniently, our antenna beamwidth (response) completely covers all extended sources of interest, namely the Sun and Moon. To obtain a 1-D intensity distribution, we simply integrate source specific intensity perpendicular to the baseline direction. For a symmetric source of small angular extent (so that we may Taylor expand in hour angle):

$$R(h_s) \approx \cos(2\pi\nu\tau_{\text{tot}}(h_s)) \int I_\nu(\Delta h) \cos(2\pi f_f \Delta h)d(\Delta h)$$

The left-hand cos term is simply the point source fringe response; the right-hand integral is a modulation function. This modulation function should predict our interferometer output's envelope curve (Figure 4).

6

The modulation function depends on the angular diameter of the source. Consider a circular source of angular radius R and uniform specific intensity; the source then has 1-D intensity profile $I_\nu(\Delta h) = \frac{1}{R}\left(R^2 - (\Delta h)^2\right)^{1/2}$. The corresponding modulation function is:

$$\mathrm{MF} = \int \frac{1}{R}\left(R^2 - (\Delta h)^2\right)^{1/2} \cos(2\pi f_f \Delta h) d(\Delta h)$$

$$\propto \frac{1}{2\pi f_f R}\left(2\pi f_f R\right) \int_0^\pi \sin^2\theta \cos\left(2\pi f_f R \cos(\theta)\right) d\theta$$

$$\propto \frac{1}{2\pi f_f R} J_1\left(2\pi f_f R\right)$$

where $J_1(z)$ is a Bessel function of the first kind [*Abramowitz and Stegun*, 1964].
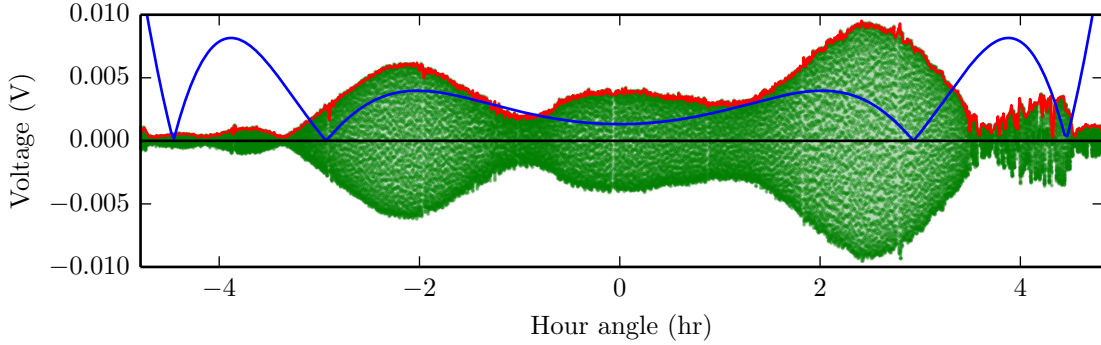

Figure 4. Shitty caption

6 Discussion

It is worth mentioning that finite frequency bandwidth contributes an extra factor of $\mathrm{sinc}(\Delta\nu\tau_{\mathrm{tot}})$ to the interferometer's extended source response. For our interferometer, the argument $\Delta\nu\tau < 1$ and so this term has a relatively small effect.
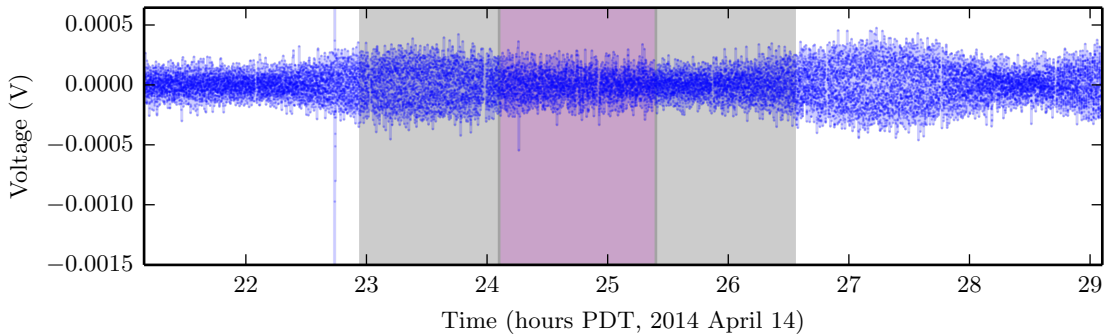
Eclipse observation.

Figure 5. Reduced interferometer data from 2014 April 14 moon observation. Partial and total eclipse times are highlighted in gray and magenta.

7 Conclusions

8 Acknowledgments

9 Electronic supplement

All supporting files are stored on the repository:
https://github.com/aarontran/ay121/lab3/.

10 References

Condon, J. J. and S. M. Ransom (2006), Essential Radio Astronomy,
    http://www.cv.nrao.edu/course/astr534/ERA.shtml.

Dutt, A. and V. Rokhlin (1993), Fast Fourier transforms for nonequispaced data, *SIAM J. Sci. Comput.*,
    14(6), 1368–1393, doi:10.1137/0914081.

Ferraz-Mello, S. (1981), Estimation of periods from unequally spaced observations, *Astrophys. J.*, *86*(4),
    619–624, doi:10.1086/112924.

Green, R. M. (1985), *Spherical astronomy*, 520pp., Cambridge Univ. Press, Cambridge.

Hafez, Y. A. et al. (2014), A radio determination of the time of the New Moon, *Mon. Not. Roy. Astron.
    Soc.*, *439*(3), 2271–2280, doi:10.1093/mnras/stt2476.

Pettit, E. and S. B. Nicholson (1930), Lunar radiation and temperatures, *Astrophys. J.*, *71*, 102–135,
    doi:10.1086/143236.

Salomonovich, A. E. and B. Y. Losovskii (1963), Radio-brightness distribution on the lunar disk at 0.8 cm,
    Soviet Astron., *6*(6), 833–839.